Parameters and scalings for dry and immersed granular flowing layers in rotating tumblers

Florent Pignatel,[1] Caroline Asselin,[2] Lucas Krieger,[2] Ivan C. Christov,[3,4,*] Julio M. Ottino,[1,3,5] and Richard M. Lueptow[1,5,†]

[1]*Department of Mechanical Engineering, Northwestern University, Evanston, Illinois 60208, USA*

[2]*French Air Force Academy, Salon de Provence, France*

[3]*Department of Chemical and Biological Engineering, Northwestern University, Evanston, Illinois 60208, USA*

[4]*Department of Engineering Sciences and Applied Mathematics, Northwestern University, Evanston, Illinois 60208, USA*

[5]*The Northwestern Institute on Complex Systems (NICO), Northwestern University, Evanston, Illinois 60208, USA*

(Received 14 March 2012; revised manuscript received 21 June 2012; published 18 July 2012)

The scaling properties of the continuous flowing layer in a quasi-2D circular tumbler half filled with a granular material are studied experimentally in the presence of three different interstitial fluids (air, water, and glycerine). In the dry case, the dimensionless flowing layer thickness δ_0/d scales with the dimensionless flow rate $Q^*_{\text{dry}} = Q/(d\sqrt{gd})$, where Q is the flow rate, d is the particle diameter, and g is the acceleration due to gravity, in agreement with previous studies. However, unlike previous studies, we show that the exponent for the power-law relation between the two depends on the range of Q^*_{dry}. Meanwhile, the angle of repose increases linearly with Q^*_{dry}. In the immersed case, the interstitial fluid changes the relevant time scales, which can be accommodated by considering the fluid properties. The result is that there are two different expressions for the dimensionless flow rate in the immersed flow; one corresponding to a free fall regime for a large Stokes number, and one corresponding to a viscous regime at small Stokes number. On this basis, a single dimensionless flow rate that incorporates both buoyancy and viscous friction is proposed. The effect of side walls is also investigated. For dry flows and those immersed in water, the thickness of the flowing layer decreases while the slope of the free surface increases as the gap separating the walls becomes smaller. For immersed granular flows with glycerine as the interstitial fluid, however, the ratio of the thickness of the flowing layer to the bead diameter is independent of the distance the between the side walls because viscous effects dominate.

DOI: 10.1103/PhysRevE.86.011304 PACS number(s): 83.80.Fg, 47.57.Gc, 45.70.−n

I. INTRODUCTION

Granular media are encountered in nature and in many industries (e.g., formation of dunes, triggering of avalanches, processing of grains, mixing of construction materials, and pharmaceuticals) [1,2]. In the present work, we consider noncohesive granular materials. Various aspects of the flow of such materials have been explored in the past two decades (see, e.g., [3–10]). A number of studies of dry granular flows have focused on quasi-two-dimensional (quasi-2D) tumblers because this system is a prototypical configuration that can readily display a number of phenomena, including chaotic mixing [5,7,11] and segregation (demixing) [12–15], the latter occurring for bidisperse (or polydisperse) particles.

When a partially filled tumbler of radius R rotates, a thin layer of fluidized material (the *flowing layer*), whose maximal thickness (typically taken at its center) is denoted by δ_0, forms at the surface of the granular material (see Fig. 1). In quasi-2D tumblers it is easy to set a steady flow rate Q by controlling the rotation rate (angular velocity ω) of the device.

Orpe and Khakhar [16] have suggested that in this system, the flowing layer thickness is essentially determined by two parameters (see also [17]): the Froude number $\text{Fr} = \omega^2 R/g$ and the ratio d/R, where g is the acceleration due to gravity and d is the particle diameter. GDR MiDi [18], on the other hand, using a portion of the data from [16,19] included herein as well as other data that is not directly comparable, found a scaling relation between the thickness of the flowing layer (measured in bead diameters) and an appropriately dimensionless flow rate: $\delta_0/d \propto \sqrt{Q^*_{\text{dry}}}$, where $Q^*_{\text{dry}} = Q/(d\sqrt{gd})$. The dependence of δ_0/d on $\sqrt{Q^*_{\text{dry}}}$ comes about from estimating the flow rate from the shear rate as $Q \propto \dot{\gamma}\delta_0^2$ and $\dot{\gamma} \propto \sqrt{g/d}$ [[18], Eq. (11)] in the portion of the flowing layer with a streamwise velocity that is approximately linear with depth. For the flow in a tumbler, Q^*_{dry} can be shown to be a combination of Fr and d/R (see Sec. III). In another set of experiments, however, Félix *et al.* [19] found that $\delta_0/d \propto \omega^n$, where n varies from 0.17 to 0.68 for R/d from 23.5 to 3700. This suggests a strong dependence of the flow on the geometry, which is not accounted for by the dimensionless parameters Fr and d/R. In fact, it is well known that side walls have a significant impact on dry granular flows on a heap in an inclined channel [20,21] and in rotating tumblers [22,23].

Determining the governing dimensionless parameters and any existing scaling relationship between them, either theoretically or experimentally, is important when addressing *scale-up* [24], that is, when one tries to extrapolate from experimental results in the laboratory to industrial-scale granular flows. Several studies have considered this issue [24–27], but most have been restricted to dry conditions. Recently, there has also been interest in the transition between dry, wetted, and immersed granular flow [28], and the effect of the interstitial fluid's viscosity on the rate of mixing [29]. While scaling laws have been proposed and verified for the dry case [18], we show that they require modification in the immersed cases.

Jain *et al.* [30] studied the influence of the interstitial fluid on the properties of granular flows in a quasi-2D tumbler. For large

*Present address: Department of Mechanical and Aerospace Engineering, Princeton University, Princeton, New Jersey 08544, USA.

†To whom correspondence should be addressed; r-lueptow@northwestern.edu

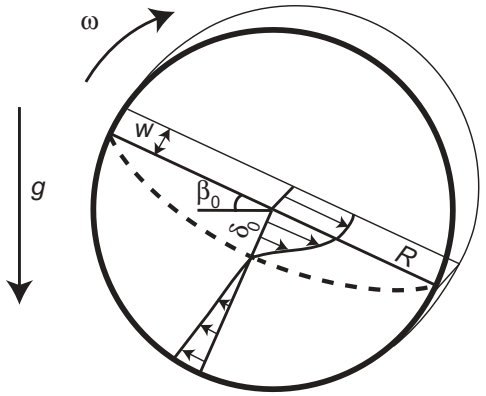

FIG. 1. Sketch of a half-full circular tumbler of radius R and the flowing layer (its lower boundary denoted by the dashed curve), which is characterized by its maximal thickness δ_0 and its dynamic angle of repose β_0 (or free surface slope $\tan\beta_0$).

steel beads ($d = 2$ mm or 3 mm), they were able to collapse the measured velocity profiles independently of the interstitial fluid. For smaller steel beads ($d = 1.2$ mm), however, the collapse under this scaling was not as good, indicating that the interstitial liquid influences the flow of small beads. This is consistent with results on granular avalanches in rotating tumblers by Courrech du Pont *et al.* [31], who showed that the different flow regimes for dry and immersed granular materials can be characterized by a Stokes number and the grain density–fluid density ratio. This approach accounts for the properties of the fluid and the particles and has been extended by Cassar *et al.* [32] to uniform flows down inclined channels.

In this study, we examine dry and immersed (wet) steady granular flows in a quasi-2D tumbler of circular cross-section. We perform experiments with air, water, and glycerine as the interstitial fluid and over a broad range of particle diameters for the monodisperse granular media. Our measurements focus on the thickness of the flowing layer δ_0 at the center of the tumbler and on the dynamic angle of repose β_0 (see Fig. 1) because these two quantities are important in characterizing the flow. For example, the thickness of the flowing layer combined with the flow rate can be used to estimate the order of magnitude of other important kinematic quantities such as the mean velocity $V \sim Q/\delta_0$ and shear rate $\dot{\gamma} \sim V/\delta_0$. On the other hand, the dynamic angle of repose is related to the properties of the particles and the flow conditions (possibly on δ_0 as well) [20,21,33,34].

The goal of this paper is to highlight the similarities and differences between dry and immersed granular flows. In the process, we are able to develop a practical scaling relationship for the flowing layer thickness in terms of the system parameters. Additionally, we explore the effect of the side walls on the proposed scaling relations.

II. EXPERIMENTAL METHOD

A. Setup

The experimental setup consists of a quasi-2D circular tumbler of radius $R = 11.4$ cm with variable axial width: $W = 6.4$ mm, 12.7 mm, 19 mm, or 25.4 mm. The tumbler was half filled with particles and rotated about its axis by a stepper motor with a gear drive controlled by a computer. The device was capable of rotation rates ω from 0.0025 rpm up to 30 rpm. The tumbler was made of five plates in the following order: one clear side wall, one chamber plate with a circular cut-out used to set W, one clear side wall, one colored plate (black or white), and one metal plate for mounting to a shaft. For the side walls, we used static dissipative cast acrylic to avoid electrostatic effects under dry conditions. The colored plate was used to enhance the visualization of the free surface of the flow. In the wet experiments, the chamber and the grains were totally immersed in liquid, so silicone O-rings were used to seal the chamber plate in order to avoid liquid leakage. The tumbler was illuminated with a spotlight placed far enough from the tumbler to prevent warming of the liquid inside. Experiments were recorded with a JVC Everio X GZ-X900 camera at 30 frames/second with a resolution of 1920 × 1080 pixels.

TABLE I. Characteristics of the particles used, where "g" stands for glass and "s" for steel.

Batch	Material	ρ_p (g/cm^3)	d (mm)
g120	glass	2.5	0.119 ± 0.017
g370	glass	2.5	0.37 ± 0.037
g1	glass	2.5	1.16 ± 0.12
g2	glass	2.5	2.14 ± 0.07
s2	steel	7.5	2.49 ± 0.07

We used glass and steel beads of different sizes with their characteristics reported in Table I. Wet experiments were performed using either water or glycerine as the interstitial medium. The viscosity of glycerine changes with the ambient temperature; for each experiment, the viscosity η_f was measured with a falling ball viscometer and is reported in Table II. We ensured that the viscosity did not change during the course of an experiment. The fluid density ρ_f is less sensitive to the ambient temperature and was measured once with a 25 ml volumetric flask.

For each set of experiments, the rotation rate ω was controlled so that the flow was in the rolling regime. The lowest ω considered was the minimum rotation rate that still results in a continuous flow (no intermittent avalanching). In the dry case, the highest ω considered was the maximum rotation rate giving a free surface that was at most weakly S-shaped. In the immersed case, on the other hand, the upper limit on ω was based on two different criteria. For very viscous fluids, the maximum rotation rate was such that no particles were carried off the flowing layer at its upstream end by the rotating wall; that is, no particles were in suspension in the fluid in the top half of the tumbler. Otherwise, the maximum rotation rate was such that the free surface was weakly S-shaped or, in some cases, such that no waves appeared on the free surface of the flowing layer. Each experiment was repeated two or three times

TABLE II. Characteristics of the interstitial liquids considered.

Liquid	ρ_f (g/cm^3)	η_f (cP)
water	0.998 ± 0.001	0.98 ± 0.03
glycerine	1.25 ± 0.01	840 ± 150

in order to ensure reproducibility and provide error bars (one standard deviation). Finally, for the smallest beads (g120), a strip of waterproof sandpaper (with average roughness of 36 μm) was applied to the circumference of the tumbler to prevent slippage of the particles with respect to the tumbler. This did not alter the characteristics of the flowing layer.

B. Measurement technique

The flowing layer was characterized by its thickness δ_0 and the dynamic angle of repose β_0, both measured at the center of the tumbler. The thickness of the flowing layer was taken to be the distance between the free surface and the fixed point in the laboratory frame of reference, which coincides with the definition of Félix *et al.* [19]. To find the location of the fixed point the total exposure time Δt was increased numerically by constructing an image in which pixel intensities are the averages of pixel intensities from a sequence of N images [35] giving $\Delta t = N \times 1/30$ s (see Fig. 2). This technique is useful for visualizing streak lines [16] and is particularly suitable for slow flowing layers because the exposure time can be easily varied to match the flow. A similar approach was used by Komatsu *et al.* [36] for visualizing creeping granular motion on a heap and by Xu *et al.* [37] to measure the flowing layer depth in a tumbler. Finally, the long-exposure image was used to measure δ_0 and β_0 as shown in Fig. 2(b).

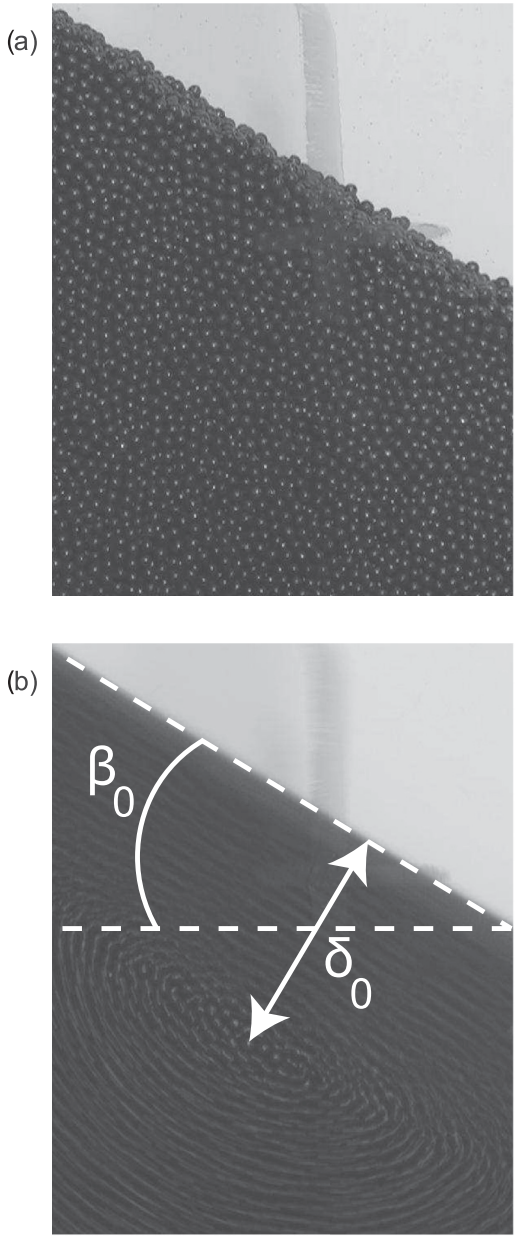

FIG. 2. Illustration of the experimental measurement method for $W = 25.4$ mm, g1 beads immersed in glycerin, and $\omega = 0.01$ rpm. (a) Single-frame exposure time $\Delta t = 1/30$ s; no particles appear to move. (b) Total exposure time $\Delta t = 70$ s. The time-exposed motion of the particles makes it possible to distinguish the flowing layer, measure its thickness δ_0, and find the free surface slope $\tan \beta_0$.

III. DIMENSIONAL ANALYSIS AND CHARACTERISTIC TIME SCALES

Eight physical quantities characterize this system. The tumbler is described by its axial width W, radius R, and rotation rate ω. The particles' properties are their diameter d and density ρ_p. The interstitial fluid is characterized by its dynamic viscosity η_f and its density ρ_f. Finally, the granular flow is driven by gravity g. A dimensional analysis indicates that five dimensionless parameters should uniquely describe the properties of the flow.

Let us first restrict to a dry system in which ρ_p, ρ_f, and η_f do not play a role. Then, one can form at most three dimensionless groups, e.g.,

$$\frac{W}{d}, \quad \frac{R}{d}, \quad \mathrm{Fr} = \frac{\omega^2 R}{g}. \tag{1}$$

As discussed in the Introduction, following GDR MiDi [18], a dimensionless flow rate can be used instead of the Froude number as the third parameter. The flow rate (per unit width) in a quasi-2D circular tumbler is

$$Q = \tfrac{1}{2}\omega\left(R^2 - \delta_0^2\right) \approx \tfrac{1}{2}\omega R^2 \quad (\delta_0 \ll R), \tag{2}$$

where the last approximation holds for flowing layers with small aspect ratios as is typically the case in the rolling (continuous flow) regime [5]. The flow rate Q can be made dimensionless by a quantity having units of length^2/time. For dry granular flow, all time scales must involve g so taking d as the length scale, we have $t = t_{\mathrm{dry}} = \sqrt{d/g}$. Therefore, the dimensionless flow rate Q^* is

$$Q^*_{\mathrm{dry}} = \frac{(1/2)\omega R^2}{d^2/t_{\mathrm{dry}}} = \frac{(1/2)\omega R^2}{d\sqrt{gd}} = \frac{1}{2}\mathrm{Fr}^{1/2}\left(\frac{R}{d}\right)^{3/2}. \tag{3}$$

Thus, a dry granular flow in a tumbler can be equivalently characterized by either the parameters in Eq. (1) or

$$\frac{W}{d}, \quad \frac{R}{d}, \quad Q^*_{\mathrm{dry}}. \tag{4}$$

For the immersed case, it is evident that a buoyancy parameter $\Delta\rho/\rho_p = (\rho_p - \rho_f)/\rho_p$ must play a role [38]. In addition, viscous effects must also be included. It has been suggested [31,32] that dense granular flows immersed in a liquid can be studied using the same framework as dry granular flows by defining an appropriate characteristic time to be used in making the flow rate dimensionless [recall Eq. (3)]. One

way to gain insight into the relevant time scales is to consider the force balance for an isolated particle falling vertically:

$$\rho_p \frac{\pi}{6} d^3 \frac{dv_p}{dt} = \Delta\rho \frac{\pi}{6} d^3 g + F_{\text{drag}}. \quad (5)$$

Here, v_p is the velocity of the particle and $F_{\text{drag}} = -3\pi\eta_f d v_p$ is the Stokes drag [[39], Sec. 4.9] experienced by the particle [40]. Note that Eq. (5) differs from Courrech du Pont *et al.* [[31], Eq. (1)], who use the apparent weight $(\pi/6)\Delta\rho d^3 g \sin\beta_0$ in order to describe macroscopic avalanches in a tumbler as a succession of elementary falling processes in the direction of the flow (hence, including $\sin\beta_0$). Equation (5) also differs from Cassar *et al.* [[32], Eq. (3)], who express the first term on the right-hand side in terms of a confining pressure instead of the gravitational force.

The solution of Eq. (5) subject to $v_p(t=0) = 0$ is

$$v_p(t) = \frac{d^2 g \Delta\rho}{18\eta_f}\left[1 - \exp\left(-\frac{18\eta_f}{d^2\rho_p} t\right)\right]. \quad (6)$$

For long times ($t \to \infty$), the particle's velocity is dominated by the viscous drag, from which we see that

$$v_p \to \frac{d^2 g \Delta\rho}{18\eta_f} = \frac{d}{t_v}, \quad t_v = \frac{18\eta_f}{\Delta\rho g d}, \quad (7)$$

giving us the *viscous time scale* t_v. Now, notice that

$$\frac{18\eta_f}{d^2\rho_p} = t_v \frac{g}{d}\frac{\Delta\rho}{\rho_p} = \frac{t_v}{t_{ff}^2}, \quad t_{ff} = \sqrt{\frac{d}{g}\frac{\rho_p}{\Delta\rho}}, \quad (8)$$

so t_{ff} can be considered as another characteristic time scale. To understand its physical meaning, suppose that $F_{\text{drag}} = 0$ in Eq. (5); then

$$v_p(t) = \frac{g\Delta\rho}{\rho_p} t. \quad (9)$$

The time it takes to travel a distance d with this velocity v_p is such that $v_p t = d$ or $t = \sqrt{d\rho_p/(g\Delta\rho)} \equiv t_{ff}$. Hence, t_{ff} is the *free fall time scale* with no drag. For the dry system, $\Delta\rho/\rho_p \approx 1$, and the free fall time scale reduces to the time scale defined above Eq. (3): $t_{ff} \approx \sqrt{d/g} = t_{\text{dry}}$.

Note that $\tau = t_{ff}^2/t_v = d^2\rho_p/(18\eta_f)$ can be considered as a third time scale that governs the transition between a free fall regime [Eq. (5) with $F_{\text{drag}} = 0$] and a viscous regime [Eq. (5) with only F_{drag} on the right-hand side]. To determine which of the two regimes the particle is in, we follow [31,32] and use a ratio of time scales to define a *Stokes number* as

$$\text{St} = \frac{t_{ff}}{t_v} = \frac{d^{3/2}\sqrt{\Delta\rho g \rho_p}}{18\eta_f}. \quad (10)$$

From the definitions of t_{ff} and t_v, we see that the flow regime is free fall (no drag) if $\text{St} > 1$, whereas the regime is viscous (drag dominated) if $\text{St} < 1$. Thus, Eq. (10) is similar to the definition of the Stokes number in the multiphase flow literature [[41], §1.2.5]; i.e., at low Stokes number the fluid–particle viscous forces dominate, while at high Stokes number particle contact forces dominate. The values of the dimensionless parameters for our experiments are given in Table III.

Now, we can adapt the expression for the dimensionless flow rate in Eq. (3) to an immersed granular flow in a tumbler.

TABLE III. The dimensionless parameters St and $\rho_p/\Delta\rho$ for the particles and interstitial fluids used in our experiments. Elements of the table are left empty when no experiments were carried out under the corresponding conditions.

		g120	g370	g1	g2	s2
air	St	30	160	900	2300	8500
water	St	0.45	2.4	14	34	150
glycerine	St			0.01	0.04	0.18
air	$\rho_p/\Delta\rho$	1	1	1	1	1
water	$\rho_p/\Delta\rho$	1.7	1.7	1.7	1.7	1.15
glycerine	$\rho_p/\Delta\rho$			2	2	1.2

In the free fall regime ($\text{St} > 1$), we replace t_{dry} by t_{ff} to obtain

$$Q_{ff}^* = \frac{\omega R^2 \rho_p^{1/2}}{2d^{3/2} g^{1/2} (\Delta\rho)^{1/2}} = \frac{1}{2}\text{Fr}^{1/2}\left(\frac{R}{d}\right)^{3/2}\left(\frac{\rho_p}{\Delta\rho}\right)^{1/2}, \quad (11)$$

and, in the viscous regime ($\text{St} < 1$), we use t_v to obtain

$$Q_v^* = \frac{9\omega R^2 \eta_f}{\Delta\rho g d^3} = \frac{1}{2}\text{Fr}^{1/2}\left(\frac{R}{d}\right)^{3/2}\left(\frac{\rho_p}{\Delta\rho}\right)^{1/2}\frac{1}{\text{St}}. \quad (12)$$

Note that the product $\text{Fr}\,\rho_p/\Delta\rho$ in Eqs. (11) and (12) also appears in scaling relation for the transition to the centrifuging regime in immersed granular flows in a tumbler [38]. We can combine Eqs. (11) and (12) into a single dimensionless flow rate:

$$Q^* \approx \frac{1}{2}\text{Fr}^{1/2}\left(\frac{R}{d}\right)^{3/2}\left(\frac{\rho_p}{\Delta\rho}\right)^{1/2}\left(1 + \frac{1}{\text{St}}\right). \quad (13)$$

Clearly, $Q^* \approx Q_v^*$ for $\text{St} \ll 1$, while $Q^* \approx Q_{ff}^*$ for $\text{St} \gg 1$.

Of course, the analysis proposed here is simplistic. When granular matter flows particles are not isolated, and we cannot ignore the influence they have on each other. Furthermore, the flow is confined meaning that the granular material acts as an effective porous medium. Cassar *et al.* [32] take into account the porosity of the medium by modifying the magnitude of the drag force acting on a single grain. However, their analysis does not immediately extend to tumblers; thus we do not consider this effect. Nevertheless, this simplified analysis based on the forces acting on a single sphere in an infinite medium has been used successfully for other types of granular flows [31,32], and, as we show below, it provides a useful approach to analyzing our experimental data as well.

IV. EXPERIMENTAL RESULTS AND DISCUSSION

A. Dry case

1. Thickness of the flowing layer

A number of studies in the literature report the thickness of the flowing layer δ_0 as a function of the various system parameters. We have collected data from [16,19,30,42,43] to supplement and compare to ours. The relevant parameters and their ranges are summarized in Table IV.

From Eq. (1), we recall that the Froude number $\text{Fr} = \omega^2 R/g$ is one parameter that can be used to describe the flow of a granular material under dry conditions, and this parameter is commonly used in the literature to classify the possible flow regimes [5,44]. Figure 3 shows the dependence of δ_0/d on

TABLE IV. Experimental parameters under dry conditions for the present study and for the studies from the literature [16,19,30,42,43], the data from which were used in generating Figs. 3 and 4.

Ref.	Material	d (mm)	R/d	W/d	Fr $\times 10^4$	$Q^*_{\rm dry}$
[42]	sugar balls	1.8	40	8	7–80	3–10
[42]	BBs (steel)	4.5	15	3	70–200	3–6
[42]	sugar crystals	1	70	15	10–40	10–20
[16]	glass beads	2	20–80	10	20–640	5–130
[16]	steel beads	2	20–80	10	20–640	5–90
[16]	sand	0.8	50–200	10	20–640	8–360
[43]	glass beads	1–3	50–140	3	0.4–4	1–10
[30]	steel beads	1–3	50–120	3	0.4–4	1–13
[19]	glass beads	0.07–2	25–3700	10–100	0.6–700	0.6–9500
here	glass beads	0.012–2.1	53–960	5.5–210	0.03–155	1–500
here	steel beads	2.49	46	10	0.3–63	0.9–12

Fr. For a given experiment (d, R, W fixed with ω as the independent variable), δ_0/d increases with Fr approximately as a power law, $\delta_0/d \propto \mathrm{Fr}^\alpha$, where α is between 0.07 and 0.33. However, there is a wide spread of the data, showing poor collapse. Data from Félix *et al.* [19] have greater values of δ_0/d (up to ≈110, compared with ≈20 in our experiments) because of the larger values of R/d considered therein (up to 3700 in Ref. [19] compared with 960 in our experiments). Meanwhile, the experiments of Orpe and Khakhar [16] not only give larger values of δ_0/d at high Froude number compared to our data, but they also measure a greater slope of free surface. This could be due to the fact that the data from [16] correspond to a strongly S-shaped free surface at high Fr, whereas we have limited our study to nearly flat free surfaces.

In the Introduction and in Sec. III, we discussed that the dimensionless flow rate per unit width $Q^*_{\rm dry} = \frac{1}{2}\omega R^2/(d\sqrt{gd})$ provides an alternative approach to plotting the data, as shown in Fig. 4. Similarly to Fig. 3, we observe that δ_0/d increases with $Q^*_{\rm dry}$, but the collapse is much better in Fig. 4 than in Fig. 3.

As with the Froude number, for a given set of experiments, we observe a power-law trend $\delta_0/d \propto (Q^*_{\rm dry})^\alpha$. This result is in agreement with previous work on dry granular flows in tumblers [18,45]. However, contrary to what is reported there, we find that the exponent α of the power law is not always 0.5 but depends on the range of $Q^*_{\rm dry}$. This result is not surprising given that the square root dependence is based on assuming that the shear rate is constant and independent of the flow rate [18]. While this is the case for flow down a heap, the rotation rate in a tumbler sets both the shear rate and the flow rate. Consequently, there is a range of values for α depending on $Q^*_{\rm dry}$, as shown in Fig. 5 for individual data sets. In general,

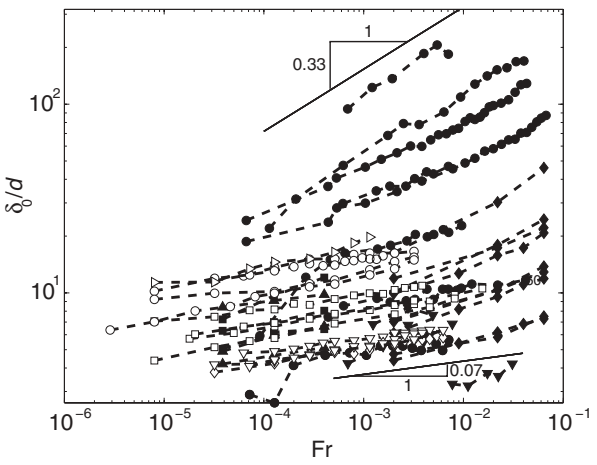

FIG. 3. Thickness of the flowing layer measured in bead diameters δ_0/d vs the Froude number $\mathrm{Fr} = \omega^2 R/g$. Data collected from previous studies: (●) corresponds to [19], (■) corresponds to [30], (♦) corresponds to [16], (▲) corresponds to [43], (▼) corresponds to [42]. Data obtained from the present study: (▷) corresponds to g120 beads, (○) corresponds to g370 beads, (□) corresponds to g1 beads, (▽) corresponds to g2 beads, and (◇) corresponds to s2 beads. Data points for each configuration (only ω varies) are linked by a dashed line to guide the eye. For clarity, error bars are not shown.

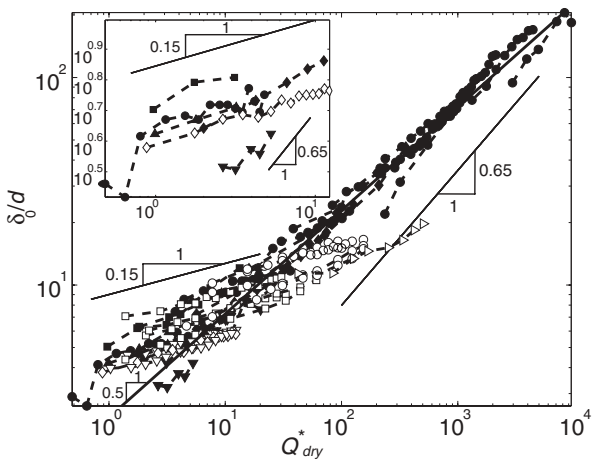

FIG. 4. The thickness of the flowing layer measured in bead diameters δ_0/d vs the dimensionless flow rate $Q^*_{\rm dry} = \frac{1}{2}\omega R^2/(d\sqrt{gd})$. Data collected from previous studies: (●) corresponds to [19], (■) corresponds to [30], (♦) corresponds to [16], (▲) corresponds to [43], (▼) corresponds to [42]. Data obtained from the present study: (▷) corresponds to g120 beads, (○) corresponds to g370 beads, (□) corresponds to g1 beads, (▽) corresponds to g2 beads, and (◇) corresponds to s2 beads. Data points for each configuration (only ω varies) are related by a dashed line to guide the eye. The inset focuses on the lowest range of $Q^*_{\rm dry}$ for each source of data. For clarity, error bars are not shown.

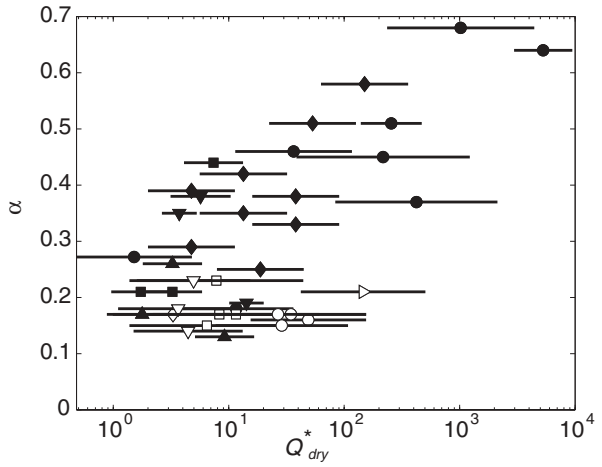

FIG. 5. Range of values of the exponent α in the scaling $\delta_0/d \propto (Q^*_{\rm dry})^\alpha$ between the dimensionless flowing layer thickness and the dimensionless flow rate for all dry data sets considered. The length of each horizontal line corresponds to the range of validity of that particular value of α. At the midpoint of each line, we have placed a symbol consistent with those in Fig. 4 to identify the data set.

α increases with the range of $Q^*_{\rm dry}$ in which a flat, continuously flowing layer occurs. Similarly, Chou and Lee [[46], Fig. 10] considered a less than half full tumbler, and though this led to a slightly different definition of $Q^*_{\rm dry}$, their data also show significant spread of α around 0.5. However, the best-fit value of α was not discussed in Ref. [46].

Because many data sets in Fig. 4 are shown at low $Q^*_{\rm dry}$, we have added an inset showing only one set of data per source. Each data set is selected so that the range of $Q^*_{\rm dry}$ is the lowest available among the data from that source. All the data at low $Q^*_{\rm dry}$ have a slope close to 0.15 except for the data from [16], which may be related to the fact that the free surface is strongly S-shaped in those experiments. At high $Q^*_{\rm dry}$, on the other hand, α is close to 0.65, though some of our g120 data suggest a lower value of α, perhaps due to electrostatic effects or slippage at the outer tumbler boundary. This result is in agreement with [19], where δ_0/d follows a power law $\delta_0/d \propto \omega^n$ with the exponent n being determined by the ratio R/d.

Furthermore, as is evident from considering individual data sets (such as those in Fig. 6, to be discussed shortly), a strict power-law relationship is valid only for individual data, and the value for α for a given data set depends on the range of $Q^*_{\rm dry}$ covered (as shown in Fig. 5). Setting aside this point, one can approximately fit a single curve through the entire collection of data sets in Fig. 4 such that $\delta_0/d \approx A(Q^*_{\rm dry})^\alpha$ with $\alpha = 0.5$ set *a priori* (even though α ranges from 0.12 to 0.68 for any particular data set), finding $A = 2.3$. A more accurate fit is $\alpha = 0.44$ and $A = 2.86$.

2. *Effect of side walls*

The precise impact of side walls on the scaling of the flowing layer thickness and an appropriate parameter to collapse the data is unknown. For example, Orpe and Khakhar [16] indicate that for $W/d \gtrsim 5$, the influence of the side walls become negligible. Similarly, Félix *et al.* [19] indicate there

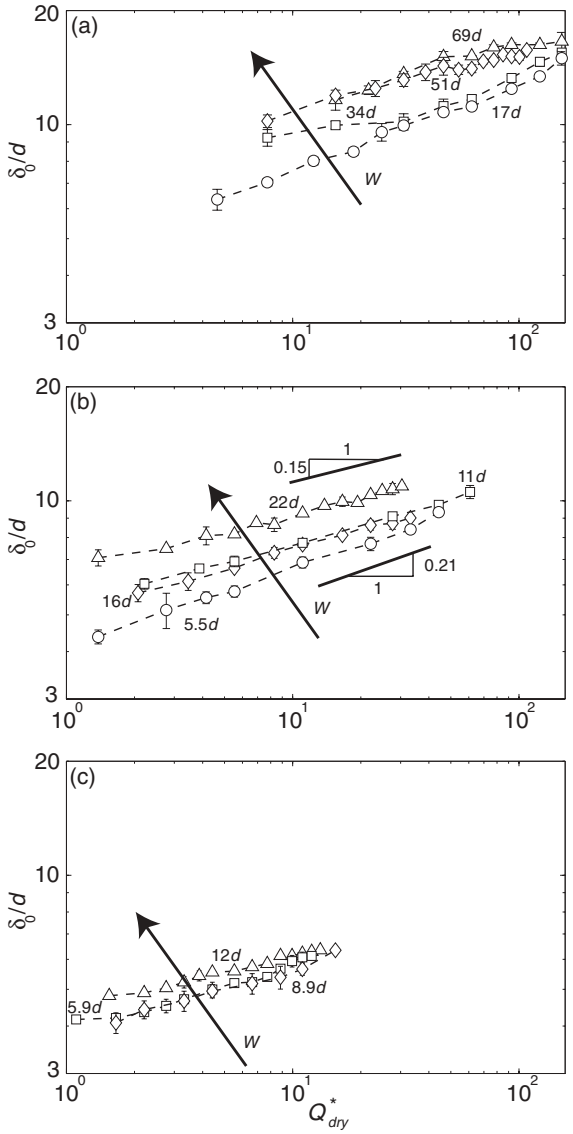

FIG. 6. Thickness of the flowing layer measured in bead diameters δ_0/d vs the dimensionless flow rate $Q^*_{\rm dry} = \frac{1}{2}\omega R^2/(d\sqrt{gd})$ for different axial widths: (○) $W = 6.3$ mm, (□) $W = 13$ mm, (◇) $W = 19$ mm, (△) $W = 25$ mm and (a) g370 beads, (b) g1 beads, and (c) g2 beads. The dashed lines are a guide to the eye. Error bars represent one standard deviation, though they may not be visible in some cases due to the size of the markers.

is no difference in the thickness of the flowing layer when varying W/d from 3 to 30 for $R/d = 50$. However, other studies have highlighted the importance of the side walls on the flow [18,20–23]. Dury *et al.* [22] performed experiments and simulations that show β_0 increases with either d/W or ω in a half-filled drum of circular cross-section; however, they did not consider the scaling with respect to dimensionless groups. Taberlet *et al.* [20] studied heap flows in a thin channel using polydisperse granular materials and a range of wall separations, showing the stability of the heap depends only on the distance W between the side walls. A similar approach was used by Jop *et al.* [21] to demonstrate that steady uniform flows on a pile are entirely controlled by friction at the side walls. For granular flows in a tumbler, Pohlman *et al.* [23] showed

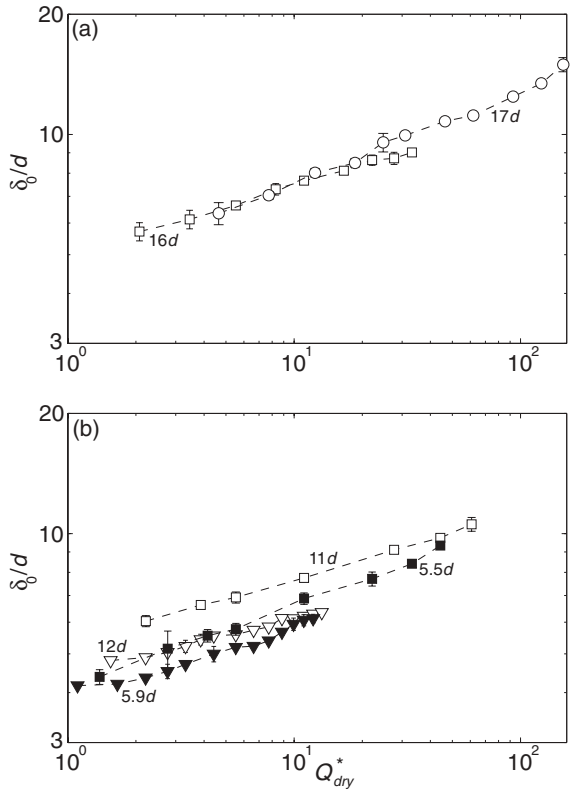

FIG. 7. Thickness of the flowing layer measured in bead diameters δ_0/d vs the dimensionless flow rate $Q^*_{\rm dry} = \frac{1}{2}\omega R^2/(d\sqrt{gd})$: (○) g370 beads, (□) g1 beads, (▽) g2 beads. In (a), open symbols correspond to $W = 16d - 17d$. In (b), open symbols correspond to $W = 11d - 12d$, while black symbols correspond to $W = 6d$. The dashed lines are a guide to the eye. Error bars represent one standard deviation.

the strong influence of side walls, specifically by measuring that decreasing the gap between the side walls can result in a factor of two increase of the streamwise velocity at the surface of the flowing layer. Similarly, GDR MiDi [18] found that the dynamic angle of repose β_0 for granular flows in rotating tumblers can increase dramatically as W is decreased.

Figure 6 focuses on the influence of the side walls on the thickness of the flowing layer for three different sizes of beads (g370, g1, and g2). Only a portion of the data from Fig. 4 is displayed for clarity. In general, as the axial width W increases, the thickness of the flowing layer increases, though in some cases [e.g., $W = 11d$ and $W = 16d$ for g1 beads in Fig. 6(b)] the ordering is imperfect.

In Fig. 7, we compare data with similar ratios W/d but different bead sizes. For the largest ratio W/d [Fig. 7(a)] the bead size seems to play no role, while for smaller ratios [Fig. 7(b)] the thickness of the flowing layer δ_0/d depends on the size of the beads. This suggests that $\delta_0/d = f(W/d, Q^*_{\rm dry})$ only when W/d is large enough, whereas $\delta_0/d = f(R/d, W/d, Q^*_{\rm dry})$ when the gap between the side walls is small. One way to motivate this observation is to note that there is some "critical value" of W beyond which the effect of the side walls on the flow changes. For example, for $W/R \lesssim 0.5$, Pohlman *et al.* [23] observed that faster shear bands near the side walls disappear. For heap flows, Courrech du Pont *et al.* [33] also found that there is a value of W beyond which the influence of the side walls is significantly weaker.

Our results can be understood by assuming a static friction force balance approach to modeling the effects of side walls for steady uniform flows [18,20,21] can be applied close to the center of the tumbler. To this end, we can write [20]

$$\frac{\delta_0}{W} = \frac{\tan\beta_0}{\mu_w} - \frac{\mu_s}{\mu_w}, \tag{14}$$

where μ_w is the Coulombic friction coefficient between the grains and the walls, and μ_s is the friction coefficient between the moving grains and the grains in the fixed bed. This equation reflects an equilibrium force balance between the weight of the grains that drives the granular flow and the friction that resists motion at the walls (μ_w) along with the friction between the moving grains and the fixed bed (μ_s).

In accordance with our experimental results (Figs. 6 and 7), Eq. (14) shows that the flowing layer is thinner when the side walls are closer together, given fixed friction properties (β_0, μ_s, and μ_w). However, the slope of the free surface $\tan\beta_0$ is coupled to the flow (in addition to the particle properties) and cannot be set independently of the flow properties (δ_0 in this case). Figure 8 shows that β_0 increases linearly with $Q^*_{\rm dry}$ for all of our data. This is different from flow down a heap, for which the slope, $\tan\beta_0$, increases linearly with $\sqrt{Q^*_{\rm dry}}$ [18], most likely because of differences in how particles enter the flowing layer in a heap (from a single source at the top of the heap) versus a tumbler (continuously along the bottom of the upstream portion of the flowing layer). In addition, note that β_0 increases faster with $Q^*_{\rm dry}$ when the gap between the walls is smaller. This is qualitatively in agreement with Eq. (14), which can be rewritten as

$$\tan\beta_0 = \mu_w \frac{\delta_0}{W} + \mu_s. \tag{15}$$

Clearly, for constant β_0, a smaller W requires a smaller δ_0, which scales with $Q^*_{\rm dry}$. This relation also implies a single value of β_0, regardless of W, for each bead size when $Q^*_{\rm dry} = 0$ (corresponding to $\delta_0 = 0$). While this is not strictly true for the data in Fig. 8, the trend towards a similar value for β_0 at $Q^*_{\rm dry} = 0$ is evident for each of the three bead sizes.

Figure 9, in which $\tan\beta_0$ is plotted versus δ_0/W, clearly illustrates the weaknesses of the relationship expressed by Eq. (15). As expected from Eq. (15), $\tan\beta_0$ increases with δ_0/W. However, the relation between δ_0/W and $\tan\beta_0$ depends on both the particle diameter d and the axial width W. Furthermore, unlike the case for flow on a heap [20], the relation is not linear, which is due to the fact that δ_0 and β_0 evolve differently with $Q^*_{\rm dry}$. Clearly, the influence of side walls in dry granular flows in a tumbler is not negligible: Friction between grains and walls reduces the thickness of the flowing layer. At the same time, because the flow rate per unit width $Q = \delta_0 V \approx \frac{1}{2}\omega R^2$ cannot change for fixed ω and R, a smaller gap between the side walls must also lead to a larger average velocity in the flowing layer.

Thus, while Eq. (14) gives a qualitative explanation of the scalings observed, it does not capture all the characteristics of the flowing layer and how it is influenced by the side walls. Nevertheless, it is possible to obtain very rough estimates of the coefficients of friction from it. The wall coefficient of friction

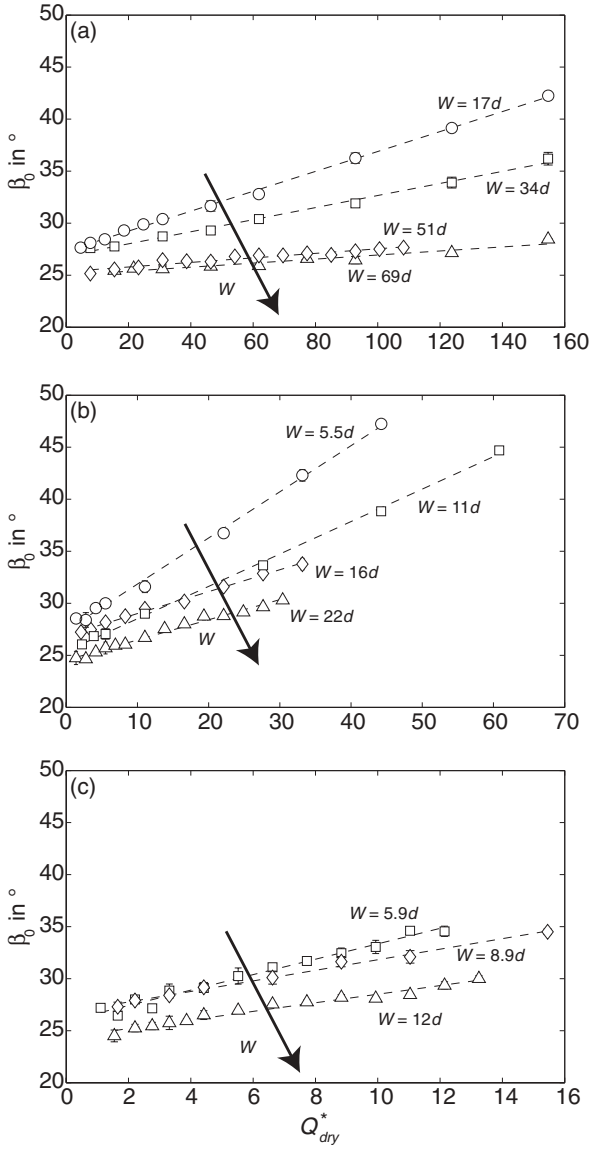

FIG. 8. The dynamic angle of repose β_0 vs the dimensionless flow rate $Q^*_{\rm dry} = \frac{1}{2}\omega R^2/(d\sqrt{gd})$ for different axial widths: (○) corresponds to $W = 6.3$ mm, (□) corresponds to $W = 13$ mm, (◊) corresponds to $W = 19$ mm, (△) corresponds to $W = 25$ mm; (a) g370 beads, (b) g1 beads, (c) g2 beads. The dashed lines are a linear fit of the data showing that β_0 increases linearly with $Q^*_{\rm dry}$. The error bars are smaller than the symbols and cannot be seen in most plots.

in most cases is $\mu_w \approx 1$, though some of the steeper slopes are nearly 3, and the more shallow slopes are as small as ≈0.2. The intercept with the vertical axis, which corresponds to μ_s, ranges from ≈0.1 to ≈0.4. Obviously, the nonlinear nature of the curves makes it difficult to obtain accurate values for μ_w and μ_s in this way.

B. Immersed case

1. Thickness of the flowing layer

Carrying out the experiments with a viscous liquid (rather than in air) as the interstitial fluid requires a substantially slower rotation rate to maintain continuous flow with a flat free surface. The thickness of the flowing layer is shown as a function of the Froude number in Fig. 10 for air, water, and glycerine. Like in the dry case (Fig. 3), the thickness of the flowing layer increases with the Froude number following a power-law trend $\delta_0/d \propto {\rm Fr}^\alpha$. In general, with our experimental set-up, the order of magnitude of δ_0/d when the grains are immersed in a fluid is close to the dry case: δ_0/d is roughly between 4 and 20. Yet, the data are widely spread. Furthermore, for a given δ_0, the data for more viscous liquids systematically correspond to a range of smaller Froude numbers.

Plotting δ_0/d as a function of the dimensionless flow rate $Q^*_{\rm dry}$ in Fig. 11 results in less scatter, particularly between water and air, but it is clear that the data from the experiments with

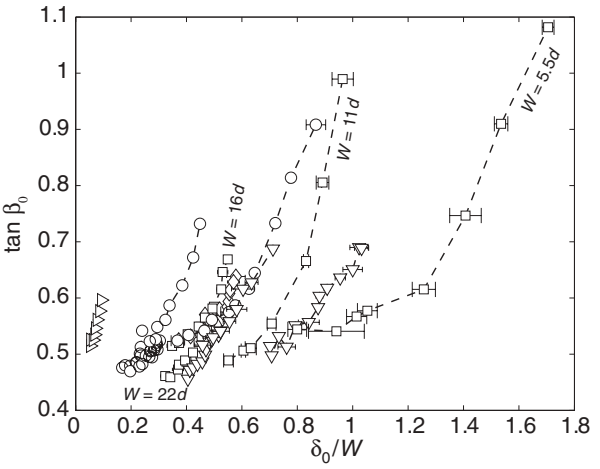

FIG. 9. Relation between the free surface slope $\tan\beta_0$ and the thickness of the flowing layer measured in axial gap lengths δ_0/W for different axial widths and different bead sizes: (▷) corresponds to g120 beads, (○) corresponds to g370 beads, (□) corresponds to g1 beads, and (▽) corresponds to g2 beads. Values for W are shown for g1 beads only. The dashed lines are a guide to the eye.

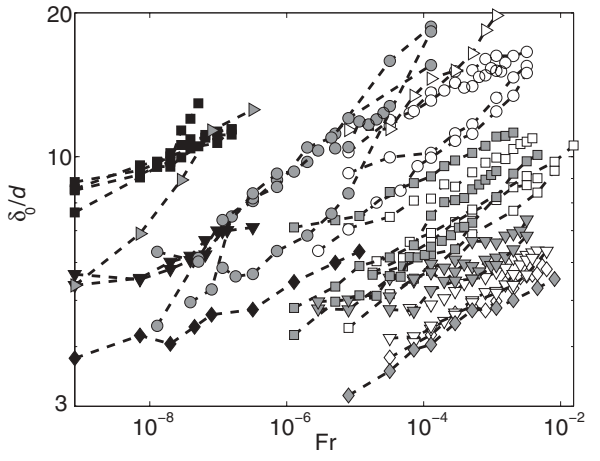

FIG. 10. Thickness of the flowing layer measured in bead diameters δ_0/d vs ${\rm Fr} = \omega^2 R/g$ for all of our data: (▷) corresponds to g120 beads, (○) corresponds to g370 beads, (□) corresponds to g1 beads, (▽) corresponds to g2 beads, and (◊) corresponds to s2 beads. Data points for each configuration (only ω varies) are linked by a dashed line to guide the eye. For clarity, error bars are not shown. Open symbols: dry; gray symbols: water; black symbols: glycerine.

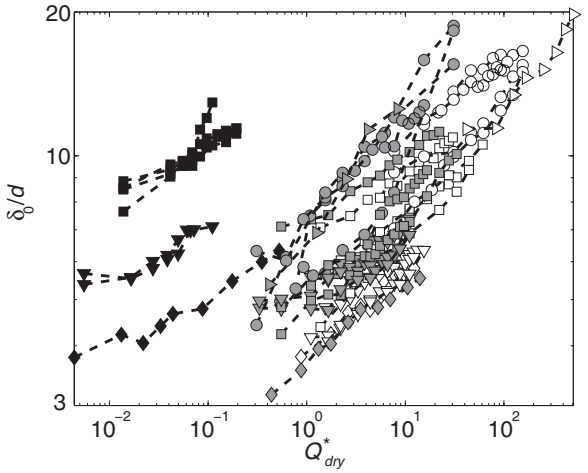

FIG. 11. Thickness of the flowing layer measured in bead diameters δ_0/d vs $Q^*_{\rm dry} = \frac{1}{2}\omega R^2/(d\sqrt{gd})$ for all of our data: (▷) corresponds to g120 beads, (○) corresponds to g370 beads, (□) corresponds to g1 beads, (▽) corresponds to g2 beads, and (◇) corresponds to s2 beads. Data points for each configuration (only ω varies) are linked by a dashed line to guide the eye. For clarity, error bars are not shown. Open symbols: dry; gray symbols: water; black symbols: glycerine.

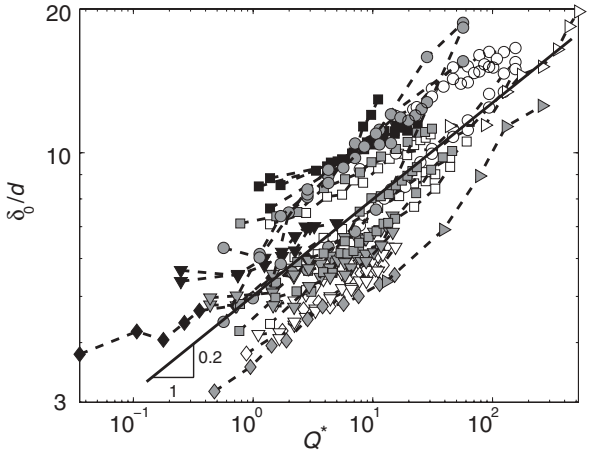

FIG. 12. Thickness of the flowing layer measured in bead diameters δ_0/d vs Q^* for all of our data, where Q^* is given by Eq. (13). Symbols: (▷) corresponds to g120 beads, (○) corresponds to g370 beads, (□) corresponds to g1 beads, (▽) corresponds to g2 beads, and (◇) corresponds to s2 beads. Data points for each configuration (only ω varies) are linked by a dashed line to guide the eye. For clarity, error bars are not shown. Open symbols: dry; gray symbols: water; black symbols: glycerine.

glycerine do not collapse onto the data corresponding to air and water. To remedy this, we can use the more general expression for the dimensionless flow rate Q^* given by Eq. (13) derived in Sec. III. The dimensionless parameters for the regimes of immersed flow for each kind of particle are reported in Table III. In glycerine, St $\ll 1$ so the regime is always viscous. In water, the Stokes number is just below 1 for the g120 beads and just above 1 for the g370 beads, whereas it is much larger for the bigger beads (g1, g2, and s2), which clearly lie in the free fall regime. Using Q^* as given by Eq. (13) accounts for both the buoyancy and viscous effects in all cases.

Figure 12 shows δ_0/d as a function of Q^* for all cases. The data gather fairly well considering that the size of the beads varies from $d = 0.1$ mm to $d = 2$ mm, both glass and steel beads are included, and the interstitial fluid's viscosity varies from $\approx 10^{-3}$ to ≈ 1 Pa · s. Very general trends can be outlined: $\delta_0/d \propto (Q^*)^\alpha$ where $\alpha = 0.12 \pm 0.05$ in glycerine, $\alpha = 0.20 \pm 0.08$ in water, and $\alpha = 0.18 \pm 0.03$ in air. The differences in α between glycerine and water must be taken as only qualitative since we were unable to carry out experiments with the small beads (g120 and g370) in glycerine because, in this case, the beads quickly became suspended even at low rotational rates. Note that for the g120 beads in water, the viscous time scale might be overestimated because the curve appears a bit too far to the right. Nevertheless, it is evident that the transition from a viscous regime to a free fall regime is around a Stokes number of one. The general trend for the data in Fig. 12, independent of the interstitial fluid, is $\delta_0/d \sim 5.1(Q^*)^{0.20}$. Of course, the collapse of the data is not as good as in Fig. 4, and the approximate trend applies to a smaller range of Q^*. However, this smaller value of α ($\approx$0.2 versus $\approx$0.5) is consistent with the low Q^* values in the exponent scatter plot in Fig. 5.

2. *Effect of side walls*

Figure 13 shows the dependence of δ_0/d on Q^* for the g1 beads with different axial widths W and the three interstitial fluids [the data for the dry case is reproduced from Fig. 6(b)]. This figure is typical of the results for all particle sizes we considered, and it illustrates the influence of the side walls on the flow with a liquid as the interstitial fluid. For flows immersed in water, the thickness of the flowing layer generally increases with W just as it does in air. Surprisingly, when the grains are immersed in glycerine, the thickness of the flowing layer does not vary significantly when W is increased from $5.5d$ to $22d$. This suggests that the walls have little impact on

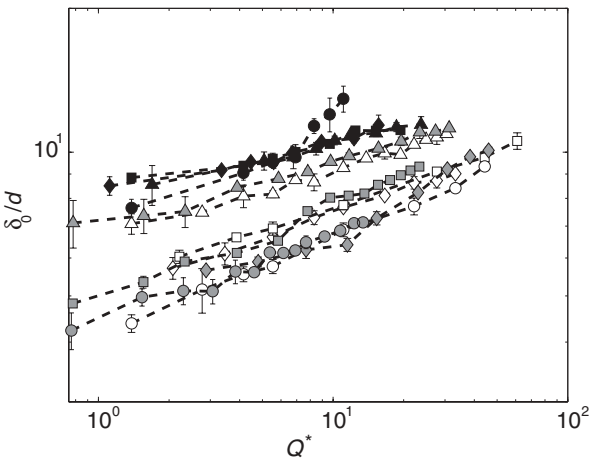

FIG. 13. Thickness of the flowing layer measured in bead diameters δ_0/d vs Q^* for g1 beads, where Q^* is given by Eq. (13). Symbols: (○) $W = 6.3$ mm ($5.5d$), (□) $W = 13$ mm ($11d$), (◇) $W = 19$ mm ($17d$), (△) $W = 25$ mm ($22d$); and empty symbols: dry case; gray symbols: water; black symbols: glycerine. The dashed lines are a guide to the eye. Error bars represent one standard deviation.

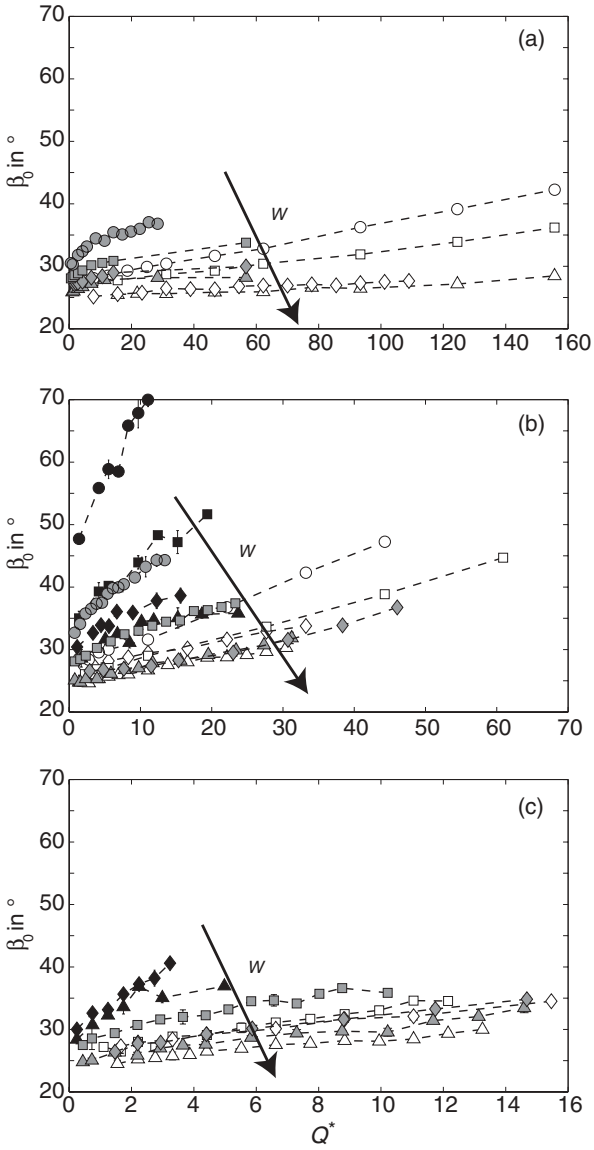

FIG. 14. The dynamic angle of repose β_0 vs the dimensionless flow rate Q^* given by Eq. (13). Symbols: (○) $W = 6.3$ mm, (□) $W = 13$ mm, (◇) $W = 19$ mm, (△) $W = 25$ mm; (a) g370 beads, (b) g1 beads, (c) g2 beads. The dashed lines are a guide to the eye. Error bars represent one standard deviation.

the thickness of the flowing layer in viscous regime, at least for this range of W, possibly as a consequence of lubrication at the walls.

Figure 14(a) shows the dynamic angle of repose β_0 for the g370 beads in air [reproduced from Fig. 8(a)] and water as a function of the dimensionless flow rate Q^*. The dynamic angle of repose β_0 increases with Q^* in both cases, but it is greater and grows faster in water than in air. Similar to the dry case, β_0 for the flow immersed in water is greater and increases faster with Q^* when the side walls are closer, though the dependence of β_0 on Q^* is not linear. Figures 14(b) and 14(c) are for the g1 and g2 beads, respectively, and also include data for glycerine as the interstitial fluid. The dynamic angle of repose β_0 increases with Q^* in all three fluids. For an equal axial width W, β_0 is greater and increases more quickly in glycerine vs water and in water vs air. Finally, in glycerine and in water, β_0 is greater and increases faster with Q^* for smaller gaps between the side walls, just as in the dry case.

In the dry case, the model based on a static force [recall Eq. (14)] was able to qualitatively capture the influence of the side walls. Similar reasoning can provide an explanation for the apparent range in the experimental data shown in Fig. 14. To do so, note that when the interstitial fluid is a viscous liquid, it exerts an additional drag on the particles in the flowing layer and at the free surface. Doppler *et al.* [34] studied the influence of a counterflow applied along the free surface of a granular flow occurring in a Hele-Shaw cell and found that the slope is increased and the granular flow is slowed down by this additional shear stress. However, the nature of our apparatus makes it difficult to quantify these additional stresses.

3. *Connection to the $\mu(I)$ rheology*

It is also tempting to interpret Fig. 14 as being equivalent to a plot of an effective friction coefficient μ as a function of a shear rate $\dot{\gamma}$ made dimensionless as, e.g., the inertial number $I = \dot{\gamma} d/\sqrt{P/\rho_p}$, where P is a confining pressure. Such an interpretation would allow a comparison to the $\mu(I)$ approach to the rheology of dense granular media [8], which has recently been extended by Boyer *et al.* [47] to cover both the dry and immersed cases. However, there are two problems with this interpretation. First, it is difficult to compute I for our tumbler flow because P is hard to measure or estimate. The second problem, as is evident from Fig. 9, is that the friction coefficient is difficult to extract because it depends on the particle size, distance between side walls, and other experimental variables.

Nevertheless, in Fig. 15 we attempt to test this idea by plotting $\tan\beta_0$, a measure of the friction coefficient, as a function of a crude estimate of the inertial number:

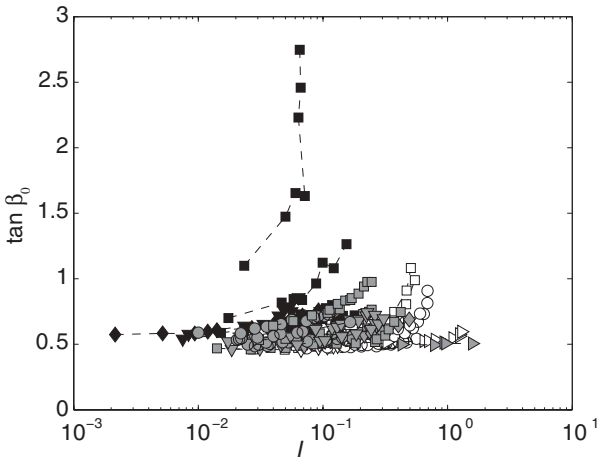

FIG. 15. The free surface slope $\tan\beta_0$ (a measure of the friction coefficient of the grains) vs a dimensionless shear rate (inertial number) for all of our data. Symbols: (▷) corresponds to g120 beads, (○) corresponds to g370 beads, (□) corresponds to g1 beads, (▽) corresponds to g2 beads, and (◇) corresponds to s2 beads. Data points for each configuration (only ω varies) are linked by a dashed line to guide the eye. For clarity, error bars are not shown. Open symbols: dry; gray symbols: water; black symbols: glycerine.

$I \approx I_v = \dot{\gamma} t_v$ or $I \approx I_{ff} = \dot{\gamma} t_{ff}$ (depending on the regime as in Ref. [32], i.e., St $\lessgtr$ 1), where t_v and t_{ff} are given in Eqs. (7) and (8), respectively, and $\dot{\gamma}$ is estimated from the flow rate as $V/\delta_0 \approx (Q/\delta_0)/\delta_0 \approx \frac{1}{2}\omega R^2/\delta_0^2$ [48]. In these plots, $\tan\beta_0$ increases monotonically with I for both dry and immersed flows. However, there is no collapse of the data across different experimental conditions.

Though Fig. 15 supports the idea that μ (in both dry and immersed flows) depends on the shear rate [8,18,32,47], there are two reasons why the $\mu(I)$ approach is not immediately applicable to the tumbler geometry. First is the significant effect of wall friction (as in Refs. [21,31]). Second is the spatial variation in the shear rate: Namely, there is a logarithmic decay of the streamwise velocity into the bulk [30,43], even though it is common to take the shear rate in the flowing layer to be constant to a good approximation. The latter is known to lead to problems in the application of the $\mu(I)$ rheology, necessitating a *nonlocal* extension of the theory [49]. Therefore, at this time, we cannot reconcile our experiments with either the "classical" dry $\mu(I)$ rheology [8,18,32] or its extension to the immersed case [47].

V. CONCLUSION

We have derived and validated through experiments new scaling relations for dry (air) and immersed (water or glycerine) granular flowing layers in quasi-2D rotating containers. In the dry case, the flowing layer thickness δ_0 and the dynamic angle of repose β_0 scale with the dimensionless flow rate $Q^*_{\rm dry}$. Unlike the results of GDR MiDi [18] and Renouf *et al.* [45] for which $\delta_0/d \propto (Q^*_{\rm dry})^\alpha$ with $\alpha = 0.5$, we found that α can vary significantly around 0.5, similarly to what Félix *et al.* [19] reported. The scaling has two well-defined regimes: one for low $Q^*_{\rm dry}$, and the other for high $Q^*_{\rm dry}$ (recall Fig. 4). In our experiments, the best fit across the entire available data set is $\delta_0/d = 2.86(Q^*_{\rm dry})^{0.44}$. The value for α is surprisingly close to 0.5, which can be obtained by estimating the flow rate based on a constant shear rate [[18], Eq. (11)]. The dynamic angle of repose of the free surface, on the other hand, increases linearly with $Q^*_{\rm dry}$. Side walls play an important role for granular flows in tumblers. When the gap between the side walls decreases, the thickness of the flowing layer decreases, but the free surface slope increases. This is a consequence of the increasing effect of wall friction on the flow.

For granular flows immersed in a viscous liquid, the dimensionless flow rate Q^* must be modified, i.e., made dimensionless using the appropriate time scale for the flow regime, to take into account the properties of the interstitial fluid. Extending recent approaches [31,32,38,50] on such scalings for immersed flows, we identified two regimes in immersed granular flows in tumblers: a free fall regime characterized by a Stokes number St $>$ 1 and a viscous regime when St $<$ 1. These regimes have different time scales, which leads to different expressions for the dimensionless flow rate. To bridge these two regimes, we proposed a dimensionless flow rate that accounts for both buoyancy in the free fall regime and viscous friction in the viscous regime:

$$Q^* \approx \frac{1}{2}\mathrm{Fr}^{1/2}\left(\frac{R}{d}\right)^{3/2}\left(\frac{\rho_p}{\Delta\rho}\right)^{1/2}\left(1+\frac{1}{\mathrm{St}}\right). \qquad (16)$$

We found that $\delta_0/d = 5.1(Q^*)^{0.20}$ is the best-fit expression for the depth of the flowing layer (based on the entire set of data in Fig. 12).

Side walls also play an important role in the immersed flows, and we can again distinguish two different regimes of how the thickness of the flowing layer scales. In the free fall regime, when the gap between the walls increases, the thickness of the flowing layer increases as it does in the presence of air as the interstitial fluid. On the contrary, we did not observe such a dependence with the axial width W in the viscous regime. This is likely due to lubrication at the side walls. In all cases, the free surface slope $\tan\beta_0$ increases with decreasing axial width W. Furthermore, the increase of the free surface slope with Q^* is stronger in glycerine than in water and air, indicating that the stresses acting on the grains are more important for very viscous interstitial fluids.

The experimental results reported in this study can be used for future work aimed at modeling dry and immersed granular flows. Specifically, this study provides useful scaling laws for granular flows in tumblers, which are frequently used practical systems for studying phenomena such as mixing, segregation, and pattern formation [51]. These scaling relationships could also be used to shed light on the practical significance of the theoretical limit of a vanishingly thin flowing layer discussed recently in connection with some new mechanisms of granular mixing [52,53]. Félix *et al.* [54] have suggested that the thickness of the flowing layer in a bidisperse granular flow in a tumbler is relevant for determining the time scale of segregation. Thus, another important question that the present approach can be used to address in the future is whether the characteristic time scales for tumblers defined in Sec. III can provide further understanding of, for example, the void-filling mechanism of segregation in gravity driven flows [55] or the "spot diffusion model" of how granular materials rearrange dynamically during flow [56]. Indeed, recent work [50] has suggested that a combination of a dimensionless flow rate and a Stokes number can provide a parameter that determines whether segregation occurs in granular slurries in rotating tumblers.

ACKNOWLEDGMENTS

I.C.C. was supported, in part, by NSF Grant No. DMS-1104047. We are grateful to Dr. Paul Umbanhowar and Dr. Umberto D'Ortona for helpful discussions. The careful reading and insightful comments by the reviewer are also much appreciated.

[1] J. Duran, *Sands, Powders, and Grains—An Introduction to the Physics of Granular Materials* (Springer, New York, 2000).

[2] B. Andreotti, Y. Forterre, and O. Pouliquen, *Les milieux granulaires: entre fluide et solide* (EDP Sciences, 2011).

[3] H. M. Jaeger, S. R. Nagel, and R. P. Behringer, Rev. Mod. Phys. **68**, 1259 (1996).

[4] P. G. de Gennes, Rev. Mod. Phys. **71**, S374 (1999).

[5] J. M. Ottino and D. V. Khakhar, Annu. Rev. Fluid Mech. **32**, 55 (2000).
[6] I. Goldhirsch, Annu. Rev. Fluid Mech. **35**, 267 (2003).
[7] S. W. Meier, R. M. Lueptow, and J. M. Ottino, Adv. Phys. **56**, 757 (2007).
[8] Y. Forterre and O. Pouliquen, Annu. Rev. Fluid Mech. **40**, 1 (2008).
[9] I. S. Aranson and L. S. Tsimring, Granular Patterns (Oxford University Press, New York, 2009).
[10] D. V. Khakhar, Macromol. Mater. Eng. **296**, 278 (2011).
[11] K. M. Hill, D. V. Khakhar, J. F. Gilchrist, J. J. McCarthy, and J. M. Ottino, Proc. Natl. Acad. Sci. USA **96**, 11701 (1999).
[12] J. C. Williams, Powder Technol. **15**, 245 (1976).
[13] F. Cantelaube and D. Bideau, Europhys. Lett. **30**, 133 (1995).
[14] D. V. Khakhar, J. J. McCarthy, and J. M. Ottino, Phys. Fluids **9**, 3600 (1997).
[15] N. Thomas, Phys. Rev. E **62**, 961 (2000).
[16] A. V. Orpe and D. V. Khakhar, Phys. Rev. E **64**, 031302 (2001).
[17] X. Y. Liu and E. Specht, Chem. Eng. Sci. **65**, 3059 (2010).
[18] GDR MiDi, Eur. Phys. J. E **14**, 341 (2004).
[19] G. Félix, V. Falk, and U. D'Ortona, Eur. Phys. J. E **22**, 25 (2007).
[20] N. Taberlet, P. Richard, A. Valance, W. Losert, J. M. Pasini, J. T. Jenkins, and R. Delannay, Phys. Rev. Lett. **91**, 264301 (2003).
[21] P. Jop, Y. Forterre, and O. Pouliquen, J. Fluid Mech. **541**, 167 (2005).
[22] C. M. Dury, G. H. Ristow, J. L. Moss, and M. Nakagawa, Phys. Rev. E **57**, 4491 (1998).
[23] N. A. Pohlman, J. M. Ottino, and R. M. Lueptow, Phys. Rev. E **74**, 031305 (2006).
[24] J. M. Ottino and D. V. Khakhar, AIChE J. **48**, 2157 (2002).
[25] Y. L. Ding, R. N. Forster, J. P. K. Seville, and D. J. Parker, Chem. Eng. Sci. **56**, 3737 (2001).
[26] A. Alexander, T. Shinbrot, and F. J. Muzzio, Powder Technol. **126**, 174 (2002).
[27] G. Weir, D. Krouse, and P. McGavin, Chem. Eng. Sci. **60**, 2027 (2005).
[28] B. Turnbull, Phys. Rev. Lett. **107**, 258001 (2011).
[29] C. C. Liao, S. S. Hsiau, and K. To, Phys. Rev. E **82**, 010302(R) (2010).
[30] N. Jain, J. M. Ottino, and R. M. Lueptow, J. Fluid Mech. **508**, 23 (2004).
[31] S. Courrech du Pont, P. Gondret, B. Perrin, and M. Rabaud, Phys. Rev. Lett. **90**, 044301 (2003).
[32] C. Cassar, M. Nicolas, and O. Pouliquen, Phys. Fluids **17**, 103301 (2005).
[33] S. Courrech du Pont, P. Gondret, B. Perrin, and M. Rabaud, Europhys. Lett. **61**, 492 (2003).
[34] D. Doppler, P. Gondret, T. Loiseleux, S. Meyer, and M. Rabaud, J. Fluid Mech. **577**, 161 (2007).
[35] We used the software ImageGrab available at http://paul.glagla.free.fr/index_en.htm.
[36] T. S. Komatsu, S. Inagaki, N. Nakagawa, and S. Nasuno, Phys. Rev. Lett. **86**, 1757 (2001).
[37] Q. Xu, A. V. Orpe, and A. Kudrolli, Phys. Rev. E **76**, 031302 (2007).
[38] G. Juarez, P. Chen, and R. M. Lueptow, New J. Phys. **13**, 053055 (2011).
[39] G. K. Batchelor, *An Introduction to Fluid Dynamics* (Cambridge University Press, Cambridge, 1967).
[40] This analysis assumes that the drag is viscous, as is the case here, since the free fall (no drag) time scale is longer than the inertial time scale.
[41] C. T. Crowe, *Multiphase Flow Handbook* (CRC Press, Boca Raton, FL, 2006).
[42] D. V. Khakhar, J. J. McCarthy, T. Shinbrot, and J. M. Ottino, Phys. Fluids **9**, 31 (1997).
[43] N. Jain, J. M. Ottino, and R. M. Lueptow, Phys. Fluids **14**, 572 (2002).
[44] J. Mellmann, Powder Technol. **118**, 251 (2001).
[45] M. Renouf, D. Bonamy, F. Dubois, and P. Alart, Phys. Fluids **17**, 103303 (2005).
[46] H.-T. Chou and C.-F. Lee, Granular Matter **11**, 13 (2009).
[47] F. Boyer, É. Guazzelli, and O. Pouliquen, Phys. Rev. Lett. **107**, 188301 (2011).
[48] Note that, equivalently, $I_{ff} = Q^*_{ff}(d/\delta_0)^2$ and $I_v = Q^*_v(d/\delta_0)^2$.
[49] K. Kamrin and G. Koval, Phys. Rev. Lett. **108**, 178301 (2012).
[50] S. H. Chou, C. C. Liao, and S. S. Hsiau, Phys. Fluids **23**, 083301 (2011).
[51] G. Seiden and P. J. Thomas, Rev. Mod. Phys. **83**, 1323 (2011).
[52] I. C. Christov, J. M. Ottino, and R. M. Lueptow, Phys. Rev. E **81**, 046307 (2010).
[53] G. Juarez, R. M. Lueptow, J. M. Ottino, R. Sturman, and S. Wiggins, Europhys. Lett. **91**, 20003 (2010).
[54] G. Félix, V. Falk, and U. D'Ortona, Powder Technol. **128**, 314 (2002).
[55] S. B. Savage and C. K. K. Lun, J. Fluid Mech. **189**, 311 (1988).
[56] M. Z. Bazant, Mech. Mater. **38**, 717 (2006).